Computational Study of the Binding Affinity and Selectivity of the Bacterial Ammonium Transporter AmtB†

Victor B. Luzhkov,* Martin Almlöf, Martin Nervall, and Johan Åqvist

Department of Cell and Molecular Biology, Uppsala University, BMC, Box 596, S-751 24 Uppsala, Sweden

Received May 31, 2006; Revised Manuscript Received July 4, 2006

ABSTRACT: We report results from microscopic molecular dynamics and free energy perturbation simulations of substrate binding and selectivity for the *Escherichia coli* high-affinity ammonium transporter AmtB. The simulation system consists of the protein embedded in a model membrane/water surrounding. The calculated absolute binding free energies for the external NH_4^+ ions are between −5.8 and −7.3 kcal/mol and are in close agreement with experimental data. The apparent pK_a of the bound NH_4^+ increases by more than 4 units, indicating a preference for binding ammonium ion and not neutral ammonia. The external binding site is also selective for NH_4^+ toward monovalent metal cations by 2.4−4.4 kcal/mol. The externally bound NH_4^+ shows strong electrostatic interactions with the proximal buried Asp160, stabilized in the anionic form, whereas the interactions with the aromatic rings of Phe107 and Trp148, lining the binding cavity, are less pronounced. Simulated mutation of the highly conserved Asp160 to Asn reduces the pK_a of the bound ammonium ion by ∼7 units and causes loss of its binding. The calculations further predict that the substrate affinity of *E. coli* AmtB depends on the ionization state of external histidines. The computed free energies of hypothetical intermediate states related to transfer of NH_3, NH_4^+, or H_2O from the external binding site to the first position inside the internal channel pore favor permeation of the neutral species through the channel interior. However, the predicted change in the apparent pK_a of NH_4^+ upon translocation from the external site, Am1, to the first internal site, Am2, indicates that ammonium ion becomes deprotonated only when it enters the channel interior.

The transmembrane uptake of ammonia and/or ammonium, the preferred source of nitrogen for many organisms, constitutes an important part of cell nitrogen metabolism. At physiological pH, the extracellular ammonia (pK_a = 9.25) is present mostly in the charged form with low permeability across nonpolar biological membranes. An important pathway of ammonium transmembrane transport is provided by the family of MEP/Amt/Rh proteins from archaea, bacteria, and eucarya (*1*−*6*). The high-affinity ammonium transporter AmtB from *Escherichia coli* has a trimeric quaternary structure, as electron microscopy of AmtB−lipid crystals to 12 Å resolution shows (*7*), and each AmtB subunit includes 11 transmembrane α-helices (*8*). Two significantly differing views of nitrogen transport arise from the studies of molecular mechanisms of Amt-mediated cell influx of NH_3 and/or NH_4^+. The first theory considers the Amt/MEP proteins as transporters of charged NH_4^+ acting via NH_4^+ uniport or H^+-coupled transfer of NH_3 (*2*, *4*, *9*−*12*). The uniport mechanism was supported recently by electric current measurements in *Xenopus* oocytes expressing the plant ammonium transporter LeAMT1;1 (*12*). The second theory is largely based on functional and structural data and underlines the role of transfer and recognition of neutral NH_3, where the Amt/MEP proteins act as mere pores and increase the rate of equilibration of ammonia across the cell membrane (*13*−*18*). Due to the controversy about the permeation mechanism, even two different definitions for Amt/MEP/Rh proteins, i.e., as ammonium transporters and ammonia channels, now exist. Mayer et al. (*19*) also argued that differing Amt/Rh channels can in fact use different nitrogen transport mechanisms.

The recently published X-ray structures of the AmtB subunit disclose key structural features which enable the protein function (*17*, *18*). The pathway for permeating ammonia is shaped by a bundle of tilted transmembrane helices and includes the extracellular and intracellular cavities connected by the narrow partially constricted internal pore that is ∼14 Å long. The broad external entrance vestibule ends up with the shallow binding site being able to accommodate either ammonium and water or methylammonium. The ligand nitrogen in the binding site is located against two aromatic rings of Phe107 and Trp148 that may prompt an important role for cation−π interactions in ligand stabilization (*17*). Functional studies of the mutant versions of ammonium transporters, including the *E. coli* AmtB, also showed a key role of a carboxyl group in position 160, proximal to the external binding site, for the channel activity and ligand recognition (*20*, *21*). The polarity of the environment for the permeating species changes when it moves to the channel interior. In particular, the surface of the internal pore involves just two H-bonded imidazoles of His168 and His318 and a number of nonpolar amino acid side chains. The pore tube is separated from the external and intracellular water-filled cavities

† Support from the Swedish Research Council (VR) and the UPPMAX computer center is gratefully acknowledged.

* To whom correspondence should be addressed. Phone: +46 18 471-5055. Fax: +46 18 530396. E-mail: vluz@xray.bmc.uu.se.

10.1021/bi0610799 CCC: $33.50
Published on Web 08/19/2006

by aromatic and aliphatic side chains, which apparently have enough space for movement to allow permeation of particles along the pore (*18*).

The crystal structures of AmtB provide a good starting point for computational mechanistic studies of the channel dynamics, acid−base equilibrium, and ligand permeation mechanisms. In particular, existing molecular simulation methods allow sufficiently accurate evaluation of the free energies for the processes involved in channel function. An important computational technique in this context is the microscopic free energy perturbation (FEP)[1] method that is based on extensive sampling of the system configurational space via molecular dynamics (MD) simulations (vide infra). The potential energies, required for solving the equations of atomic motions and for free energy calculations, are described by analytical molecular mechanics force fields. Previously, the FEP/MD method has been successfully applied in studies of permeation mechanisms for the KcsA channel (*22*, *23*) and aquaporin (*24*). The energetics of ligand interactions with the AmtB channel have been addressed by means of molecular mechanics (MM) and finite-difference Poisson−Boltzmann (PB) calculations (*18*) and a quantum mechanical MP2 method (*25*). However, the latter approaches do not consider thermal motions of the ligand and protein atoms and use a simplified description for the surrounding solvent. The aim of this work is to evaluate the NH_3 and NH_4^+ binding free energies and selectivity by means of the FEP/MD molecular simulation technique and to explore structural features of *E. coli* AmtB which determine substrate binding and permeation.

METHODS

Simulation Model. The studied system includes a single AmtB subunit (PDB entry 1U7G) immersed in a layer of octane molecules (∼34 Å thick) and solvated by water molecules at the extracellular and intracellular sides. The simulated channel contains NH_4^+ at the external binding site and three NH_3 molecules in the internal pore. Molecular simulations are performed with the parallel version of the MD program Q (*26*) using the OPLS-AA force field (*27*) and the TIP3P water model.

In the first stage, the system was modeled as a "protein−octane−water" box with dimensions of 71.4 Å × 71.4 Å × 77.6 Å, where initial packing of octane molecules around the channel was produced using Packmol (*28*). The system was made electrically neutral by compensating the excess negative charges of AmtB at the outer side and the excess positive charges at the inner side with sodium and chloride counterions. Direct nonbonded cutoffs in the periodic box calculations were 10.0 Å for protein−solvent and solvent−solvent interactions, 15.0 Å for the protein−protein interactions, and 35.0 Å for interactions of the ligand with the surroundings. Beyond these cutoffs and up to an interaction distance of 35.0 Å, the local reaction field (LRF) is approximated by the first four terms in a multipole expansion of the electrostatic effect from the surrounding (*29*). The simulated box was stepwise heated to 300 K during constant-volume MD, and the simulation was then continued with a constant-pressure MD/Monte Carlo algorithm (*30*) to attain the correct density. Subsequently, constant-volume MD equilibration was carried out for a total simulation time of 500 ps with a temperature coupling constant (τ_T) of 0.2 ps and a time step of 1 fs.

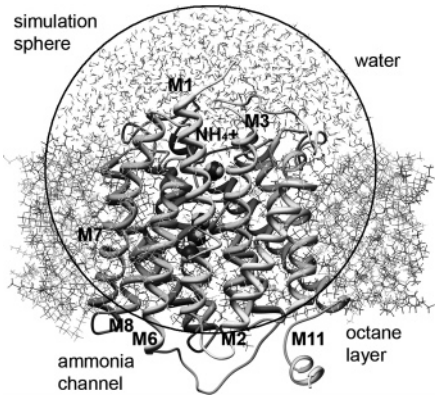

FIGURE 1: Model system, which includes the NH_3/NH_4^+ ligands, the AmtB channel with the transmembrane helices M1−M11, an octane layer, and water molecules. The drawn sphere delineates part of the whole system included in the spherical model used for free energy calculations.

In the second stage, free energy calculations were performed for a spherical model system with a radius of 30 Å, the starting structure for which was obtained from the equilibrated protein−octane−water box. The center of the simulated sphere was at the experimental external binding position of NH_3 and/or NH_4^+ (Figure 1). Protein atoms in the inner 25 Å radius sphere were not subject to any restraints, while the octane atoms in the same region were restrained with a small force constant of 0.5 kcal mol^{-1} Å^{-2}. The positions of protein and octane atoms in the spherical layer between 25 and 30 Å from the center and outside the 30 Å radius sphere were restrained by force constants of 10.0 and 100.0 kcal mol^{-1} Å^{-2}, respectively. The simulated system was made electrically neutral by adding sodium counterions in the necessary cases. The reference calculations for ligands in water were also performed with a 30 Å radius water sphere, and spherical water boundary restraints according to the surface-constrained all-atom solvent (SCAAS) model (*26*, *31*) were applied in both protein and water simulations. The simulated system was equilibrated for 500−1000 ps prior to free energy calculations.

Free Energy Calculations. Calculations of the relative free energies between the system states follow the standard FEP/MD protocol described elsewhere (*32*−*34*). In particular, the relative binding free energy ($\Delta\Delta G_{bind}$) of ligands A and B is evaluated from the conventional thermodynamic cycle for ligand transformations in water and the channel

$$\Delta\Delta G_{bind}(B-A) \equiv \Delta G_{bind}(B) - \Delta G_{bind}(A) = \Delta G_{mut}^{prot} - \Delta G_{mut}^{wat} \quad (1)$$

where ΔG_{mut}^{prot} and ΔG_{mut}^{wat} are the relative free energies for the alchemical ligand A → B "mutation" in the channel complex and in water. Such a scheme provides a consistent treatment of the states with the protein-bound ligands and the free ligands in solution. It is worth noting in this respect that another frequently used computational approach, the potential of mean force method, in practice evaluates relative

[1] Abbreviations: MD, molecular dynamics; FEP, free energy perturbation; MM, molecular mechanics; PB, Poisson−Boltzmann; LRA, linear response approximation.

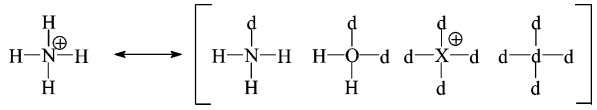

FIGURE 2: Ligand transformations involved in the FEP calculations. X and d represent the metal ion and dummy atoms, respectively.

free energies only along a limited reaction path (e.g., ion translocation within the KcsA channel pore, ref 35) and thus may not provide a proper reference free energy for the considered states (e.g., discussion in refs *24* and *36*). The FEP/MD simulation protocol used in this work involves ligand transformations in 100 steps, controlled by the mapping parameter, λ_m. The corresponding calculations of the free energy increments at each value of λ_m include equilibration for 0.5 ps and subsequent data collection for 2.5 ps. For each mutation, three to six FEP/MD simulation runs, starting from different points along the equilibration trajectory, were carried out as a rule. Such averaging over several simulation trajectories gives a useful additional estimate of the accuracy of the FEP calculations. The ligand mutations involve variations of nonbonded parameters as well as changes in the bond lengths and valence angles that are considered (Figure 2). A soft-core correction for the Lennard-Jones potential (*37*) was applied for the atom-vanishing transformations, and the mutations of the electrostatic and nonpolar parameters in the latter case were uncoupled. In the channel simulations, the coordinates of the bound ligands were harmonically restrained to the experimental values with a force constant of 3 kcal mol^{-1} Å^{-2}. The FEP/MD trajectories were calculated at 300 K with a τ_T of 0.1 ps, and a time step of 2 fs, and bond lengths were constrained using the SHAKE procedure. The computed solvation and binding free energies from FEP were additionally corrected for ion−solvent electrostatic interactions outside the simulation sphere using a macroscopic Born term with the dielectric constant of water ($\epsilon_w = 80$).

It was also interesting in selected cases to analyze the physically differing components of the computed binding free energies. Such an analysis is strictly not possible for $\Delta\Delta G_{bind}$ from the FEP method but can be performed using the expression for the free energy difference between two states, A → B, derived from the linear response approximation (LRA) (*38*, *39*)

$$\Delta G^{LRA}(B-A) = \frac{1}{2}(\langle U_B - U_A\rangle_A + \langle U_B - U_A\rangle_B) \quad (2)$$

This formula is applied only to the end points of the whole set of intermediate states generated during FEP simulations in the channel and water. We include both electrostatic and nonpolar terms in the average potential energies of eq 2, although the latter should, in principle, be scaled with a coefficient other than $^1/_2$ (*26*, *39*).

Calibration of the Force Field Parameters. The accuracy of computer simulations of ligand binding free energies relies to a large extent on properly calibrated ligand force field parameters. The original OPLS-AA parameters for the ammonia species were derived from MC simulations of ammonium ion hydration energies in a small water box (*40*) and relative hydration energies of neutral amines (*41*), both using small cutoffs. Initially, we found that the use of the standard OPLS-AA parameters gives significantly deviating hydration free energies compared with experiment for NH_3 and NH_4^+. Similar problems with the force field that was employed were also noted in a recent study of hydration free energies of neutral amines using the thermodynamic integration approach (*42*). Therefore, we recalibrated the nonbonded parameters for NH_3 and NH_4^+ to obtain more accurate hydration energies with the FEP/MD method using the SCAAS spherical boundary conditions and the LRF treatment for the long-range electrostatic interactions. In the case of neutral ammonia, we retained the original Lennard-Jones parameters, which were previously adjusted according to the experimental density (*41*), whereas the charge on the N atom is changed from −1.020 to −1.194. For ammonium ion, the σ parameter for N was increased from 3.25 to 3.51, and the partial atomic charges (−0.728 for N) were taken from the earlier ab initio RESP calculations (*43*). The computations with the recalibrated OPLS-AA parameters give significantly improved hydration free energies (Table 1). In particular, the ΔG^{wat}_{mut} for the mutations of NH_4^+ to Na^+ and Cs^+ only deviates from the experimental values by ∼0.1 kcal/mol, and that for mutation to neutral NH_3 and H_2O deviates by ∼1 kcal/mol. The latter entries in Table 1 include the Born correction mentioned above.

Table 1: Relative Hydration Free Energies (kilocalories per mole) for Ammonium Ion and Ammonia

	FEP/MD calculations[a]		
mutation	ΔG^{wat}_{mut}, standard parameters[b]	ΔG^{wat}_{mut}, calibrated parameters[c]	experiment (*44*−*46*)
$NH_3 \rightarrow H_2O$	−4.4	−2.0	−2.0
$NH_4^+ \rightarrow NH_3$	84.2	76.8	75.8
$NH_4^+ \rightarrow H_2O$	79.3	74.9	73.8
$NH_4^+ \rightarrow Na^+$ [d]	−13.5	−18.2	−18.1
$NH_4^+ \rightarrow Cs^+$ [d]	17.1	12.3	12.3

[a] The standard error of FEP calculations in water simulations, from forward−backward convergence and multiple trajectory sampling, is ≤0.4 kcal/mol. [b] Regular OPLS-AA nonbonded parameters for the nitrogen atom (N) in ammonium ion are: $q = -0.400$, $\sigma = 3.25$, and $\epsilon = 0.170$ (*40*). For NT in ammonia, they are: $q = -1.020$, $\sigma = 3.42$, and $\epsilon = 0.170$ (*41*). [c] The recalibrated OPLS-AA nonbonded parameters for N in ammonium ion are: $q = -0.728$, $\sigma = 3.51$, and $\epsilon = 0.170$. For N in ammonia, they are: $q = -1.194$, $\sigma = 3.42$, and $\epsilon = 0.170$. [d] Calculations using the nonbonded parameters for metal ions given elsewhere (*47*).

RESULTS AND DISCUSSION

The periplasmic part of the AmtB subunit forms a broad entrance vestibule for the transported species (Figures 1 and 3). In discussing the affinity of the AmtB channel for different species, it is worth noting the presence of a net negative charge at the external surface, mentioned elsewhere (*17*). In particular, there are seven external negatively charged groups (Asp6, Asp9, Glu70, Glu87, Glu225, Glu344, and Glu357) and three positively charged ones (the N-terminus, Lys7, and Lys84). However, the permanently ionized groups are fairly far (∼15−26 Å) from the NH_3 or NH_4^+ position at the external binding site (Figure 3). The channel surface near and in the binding pocket is only lined by several oxygen atoms with partial negative charges and the aromatic rings of Phe103, Phe107, and Trp148. The exception is the conserved and buried Asp160, located ∼8 Å from the binding site. A certain ambiguity can be noticed in the overall charge

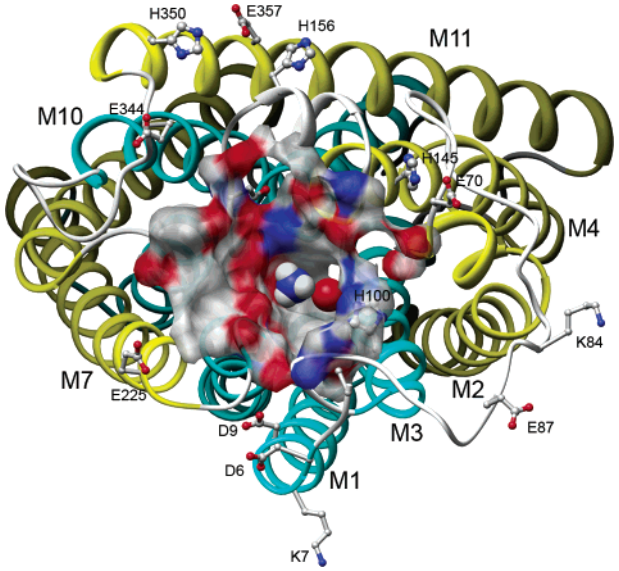

FIGURE 3: Axial view of the external part of AmtB, including the binding cavity with bound NH_4^+ and water. Ionizable amino acids are explicitly shown. The internal pore-forming helices are colored cyan.

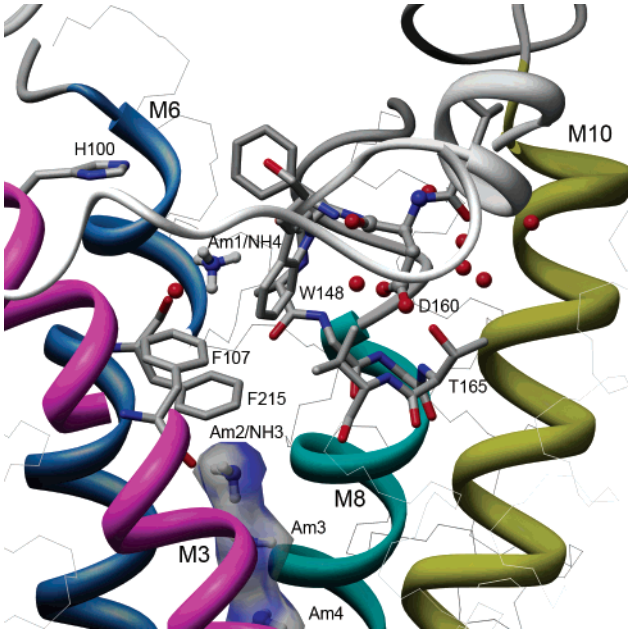

FIGURE 4: Side view of the external binding site of AmtB, including functionally important amino acids near experimental ammonia positions Am1 and Am2.

balance in the periplasmic part of AmtB from *E. coli* due to four histidines (His100, His145, His156, and His350), which have an imidazole pK_a of ~6 and can therefore change their ionization state in the operative pH range of 5.5−8.5 for ammonia channels. In the simulations below, we consider two differing situations. First is the "high-pH" condition, corresponding to the upper pH values in the ammonia channel operative range where the imidazoles are uncharged. The second case refers to the "low-pH" model in which all four external histidines are charged.

Ionization States of Asp160. An important role in ammonia transport is played by aspartic acid in position 160 (*8*, *20*, *21*), proximal to the external binding site and the permeation pore (Figures 3 and 4). Asp160 is buried inside the protein and spatially separated from the bound external NH_3 or NH_4^+ by Trp148, Ala162, and Gly163. The carboxyl oxygen atoms of Asp160 are located in a cage of five backbone NH groups from Ala162 to Val166. Besides, several water molecules are found near Asp160 in the crystal structure. The apparent pK_a of a charged amino acid can in general vary significantly, depending on the protein microenvironment. A corresponding example, related to membrane channels, is given by Glu71 in KcsA, which is buried in the water-filled pocket near the K^+ permeation pore and is unionized (protonated) in the ground state as shown by molecular simulation studies (*48*, *49*). It is therefore important to clarify the ionization state of Asp160 in AmtB.

The pK_a of Asp160 is evaluated from the difference in protonation free energies for the carboxylate group in water and protein, as described elsewhere (*48*, *50*)

$$\Delta pK_a = \frac{1}{2.3RT}[\Delta G^{wat}_{mut}(D^- \rightarrow DH) - \Delta G^{prot}_{mut}(D^- \rightarrow DH)] \quad (3)$$

Simulations of aspartic acid in water involve the reversible transformation of the side chain carboxylate ion to the uncharged protonated state. Simulations in AmtB are performed under the low-pH conditions with either NH_4^+ or H_2O in the external binding site. The computed protonation free energies are given in Table 2. For selected cases of channel simulations, the forward−backward FEP hysteresis is less than 1 kcal/mol and is paralleled by the good overall reversibility of the MD trajectories for the Asp160 microenvironment. However, in some cases, the FEP hysteresis has higher values (~13−15 kcal/mol), in which case the protein−water structure near Asp160 shows minor deviations from the initial geometry after completion of the mutation cycle. Even stronger FEP hysteresis, ~20−25 kcal/mol, was reported elsewhere (*49*) for deprotonation of Glu71 in KcsA. The carboxylate ion of Asp160 is preferentially protonated at OD2 (as defined in the original PDB structure, 1U7G) due to stabilizing interactions with the side chain oxygen atom of Thr165. The pK_a change in the protein is calculated from mutation free energies in protein and water using eq 3. The results of our simulations show that the anionic form of Asp160 is stabilized in AmtB compared to that in solution (Table 2). For the case of the water-filled recruitment cavity, the apparent pK_a of Asp160 is lower than the normal pK_a of Asp in water by 0.3−5.1 units. The presence of NH_4^+ at the external binding site produces an even more negative shift in the apparent pK_a of Asp160 due to stabilizing electrostatic interactions.

Table 2: Calculated Protonation Free Energies and the Corresponding Changes in pK_a for Asp160[a]

AmtB model	ΔG^{prot}_{mut} (kcal/mol)[b]	ΔpK_a
water-filled cavity	69.0−75.5	−0.3 to −5.1
NH_4^+ bound	81.2	−9.2

[a] Both ΔG^{wat}_{mut} and ΔG^{prot}_{mut} include the macroscopic Born correction for the 30 Å radius sphere. It may also be noted that the Born term, derived for a water surrounding, may overestimate the long-range electrostatic correction in a nonpolar membrane. However, since the binding site lies at the border of water and the membrane slab, the membrane-related correction should be close to zero (e.g., ref *51*). [b] The lower value for ΔG^{prot}_{mut} with a water-filled external vestibule is obtained when the backward runs with large hysteresis are omitted.

Table 3: Absolute and Relative Binding Free Energies (kilocalories per mole) of NH_4^+ and NH_3 at the External Cavity of AmtB

	low pH	high pH					
mutation	$\Delta\Delta G_{bind}^{FEP}$ [a]	$\Delta\Delta G_{bind}^{FEP}$ [a]	$\Delta\Delta G_{bind}^{LRA}$ [b]	ΔG_{el}^{prot}	ΔG_{el}^{wat}	ΔG_{np}^{prot}	ΔG_{np}^{wat}
dummy → NH_4^+	1.7	−7.3	−4.1	−93.6	−89.9	20.0	20.4
H_2O → NH_4^+	2.0	−5.8	−3.4	−74.2	−71.4	6.0	6.7
H_2O → NH_4^+, D160N[c]	−	4.3	3.6	−66.6	−71.4	5.5	6.7
NH_3 → NH_4^+	−	−6.0	−9.4	−77.8	−68.5	1.4	1.5

[a] The FEP binding free energy $\Delta\Delta G_{bind}^{FEP}$ is computed using eq 1. The mutation free energies in water ΔG_{mut}^{wat} (NH_4^+ → H_2O, NH_3) are given in Table 1, while the computed ΔG_{mut}^{wat} (dummy → NH_4^+) is −82.4 kcal/mol. The standard error for ΔG_{mut}^{prot} is ≤1.2 kcal/mol. [b] The LRA binding free energy $\Delta\Delta G_{bind}^{LRA}(B-A) = \Delta G_{mut}^{LRA,prot} - \Delta G_{mut}^{LRA,wat}$ is expressed as $(\Delta G_{el}^{prot} - \Delta G_{el}^{wat}) + (\Delta G_{np}^{prot} - \Delta G_{np}^{wat})$, where ΔG_{el}^{prot}, ΔG_{el}^{wat}, ΔG_{np}^{prot}, and ΔG_{np}^{wat} are the electrostatic and nonpolar contributions to ΔG^{LRA} of eq 2 in protein and water, respectively. [c] Calculations for the D160N mutant AmtB channel.

Ammonium Binding Free Energies and Selectivity of the External Binding Site. The central question in studies of the molecular mechanisms of AmtB concerns the ionization state of the transported nitrogen species. To shed new light on this issue, we evaluate here the binding free energies for charged and neutral ammonia at the external binding vestibule. The FEP/MD calculations of the relative binding free energies ($\Delta\Delta G_{bind}^{FEP}$) using eq 1 provide two ways of evaluating the absolute binding affinities as well. The first involves mutation of the ligand to dummy species, whereas the second one involves transformation to a water molecule. The two schemes are physically equivalent since they describe similar final states (although in a differing way) where water molecules occupy the binding site after the ligand is removed.

The computed absolute binding free energy of NH_4^+ in AmtB for the high-pH model is −7.3 kcal/mol from the NH_4^+ ↔ dummy mutation and −5.8 kcal/mol from the NH_4^+ ↔ H_2O mutation (Table 3). These values are in very good agreement with the experimental binding affinity of AmtB estimated from the response binding constant, K_m (≈10 μM) (*17*). Binding of NH_4^+ to AmtB in the low-pH model is energetically unfavorable by 1.7−2.0 kcal/mol, and the largest effect in this case is due to the charged His100 (Figures 3 and 4), located ∼8 Å from the binding site. The difference in the computed FEP/MD binding free energies at high pH for the NH_3/NH_4^+ pair is 6.0 kcal/mol (the apparent pK_a of NH_4^+ shifted by 4.4 units). This clearly indicates that ammonia binds to the channel in the charged form. It is of interest also to compare the binding affinities of NH_4^+ for the wild-type channel and the channel mutated at the functionally important Asp160. The free energy simulations for the chosen Asp160Asn mutant, where the carboxylate ion is replaced with a structurally similar but neutral amide group, were performed separately using the same protocol that was used for wild-type AmtB. The considered amino acid replacement produces a significant positive shift of ∼10 kcal/mol to the binding free energy (loss of binding) as calculated from the NH_4^+ ↔ H_2O transformation (Table 3). The positions of amino acids which belong to the binding site are fairly similar for the mutant and wild-type channel simulated trajectories (cf. also the earlier described FEP/MD results for the Asp^- ↔ AspH transformation in position 160). Hence, the structural effects of the Asp160 mutation, argued elsewhere (*17*), are apparently less important than the replacement of the negative charge. The provided computational results fully support the experimental data for the Asp160Ala, Asp160Asn, and Asp160Glu mutant channels, demonstrating an essential role of the carboxyl group in position 160 for ammonium uptake (*20, 21*).

The nature of the important contributions to the computed binding free energies can be explored from the energy component analysis using eq 2 (Table 3). The LRA scheme of eq 2 apparently provides a less accurate estimate for the mutation free energies than the rigorous FEP approach of eq 1. However, the relative binding free energies computed from the LRA scheme ($\Delta\Delta G_{bind}^{LRA}$) still agree quite well with those from the FEP calculations (Table 3). Inspection of the ΔG^{LRA} components shows that ammonium ion is stabilized in the channel-bound state mainly by electrostatic interactions. The differences in electrostatic contributions also determine the loss of NH_4^+ binding in the Asp160Asn mutant as well as the lower affinity of NH_3 in the wild-type channel.

The role of selected chemical groups in ligand stabilization can be accessed from straightforward calculations of the average potential energies for nonbonded interactions, $\langle E_{nb}\rangle$. Here we provide the values for $\langle E_{nb}\rangle_A$ from the same trajectories that were used in the calculations of the ΔG^{LRA} contributions of Table 3. The $\langle E_{nb}\rangle_A$ values (kilocalories per mole) of NH_4^+ with selected amino acids from the external binding site are −10.5 for Phe107, 1.3 for Val147, −7.6 for Trp148, −44.4 for Asp160, −7.9 for Phe161, −12.8 for Ala162, −7.3 for Phe215, and −16.9 for Ser219, and the total $\langle E_{nb}\rangle_A$ is −158.2. The latter energies are the sums of the electrostatic and nonpolar terms; however, the electrostatic contribution is the largest one in all cases. For Phe107 and Trp148, only the interactions with the aromatic rings are taken into account. The aromatic rings of Phe107 and Trp148 preserve a face orientation to the bound species in the computed MD trajectories. The given type of spatial arrangement could possibly suggest that the aromatic groups play a crucial role in stabilization of the bound cation as recently argued in ref *25*. However, the provided energy series clearly shows that the interaction of the ligand with the carboxylate ion of Asp160 has a much lower energy than the interactions with the aromatic rings. The second important interaction is the one with the side chain of Ser219, while the aromatic rings of Phe107 and Trp148 provide stabilization similar to that of carbonyls of Phe161, Ala162, and Phe215. The earlier reported quantum mechanical MP2 energies of the interactions of NH_4^+ with the side chains of Phe107, Trp148, and Ser219 are −10.9, −17.4, and −18.9 kcal/mol, respectively (*25*). The latter values are fairly close to the MD average interaction energies, except for Trp148, where the $\langle E_{nb}\rangle_A$ is apparently underestimated. Thus, the computational and experimental results show that the stabilization of the ammonium species at the external binding site of AmtB cannot be attributed mainly to cation−π interactions, and on the contrary, the greater part of it stems

Table 4: Relative Binding Free Energies (kilocalories per mole) and Inhibitory Activity for Monovalent Metal Cations

ion	ionic radius (Å)[a]	uptake activity (*10*)[b]	ΔG_{mut}^{prot} [c]	$\Delta\Delta G_{bind}^{FEP}$
Li^+	2.08	30	−40.0	3.3
Na^+	2.36	−	−13.8	4.4
K^+	2.80	26	1.8	2.6
Rb^+	2.89	33	7.2	2.5
Cs^+	3.14	25	14.7	2.4
NH_4^+	2.80−3.10	3.6	−	−

[a] Experimental "ion−water oxygen" distances (*52*, *53*). [b] Rates of uptake of 0.5 mM methylammonium in the presence of 10 mM inhibitor ions for the Mep2 ammonium transporter (*10*), in which case the control activity is 30. [c] Computed from the "$NH_4^+ \rightarrow$ metal ion" FEP mutations for the "high-pH" AmtB channel model.

from the essential electrostatic interactions of the ligand with the negatively charged Asp160 and several other polar chemical groups.

We have also explored the selectivity of the external cavity of AmtB toward several monovalent metal cations. The binding pocket for external ammonium has an elongated shape and in principle is able to fit ligands with more than one heavy atom (Figure 3). In the narrowest part, the geometric dimensions of the cavity are determined by the minimal distance between the side chain heavy atoms of Ser219 and Phe103 with those of Trp148 (5.7−7.2 Å in the 1U7G structure). Such a structural arrangement differs from the symmetric external binding site and permeation pore in tetrameric K^+ channels. The FEP/MD calculations show that the external cavity favors binding of NH_4^+ among other ions by several kilocalories per mole (Table 4). The predicted increase in K_d (compared to that of ammonium ion) varies from ∼56-fold for Cs^+ to ∼1600-fold for Na^+. The computed difference in the $\Delta\Delta G_{bind}^{FEP}$ generally lessens with the increase in the metal ion size that qualitatively agrees with the data on the methylammonium uptake inhibition in the Mep2 channel (Table 4). However, the average N−O distance for NH_4^+ in water can be compared to experimental mean ion−water distances of 2.80−3.14 Å for K^+, Rb^+, and Cs^+ (Table 4). Overall, the computed $\Delta\Delta G_{bind}^{FEP}$ values are determined by a fine balance between the electrostatic and van der Waals interactions of the ligand with the protein and water surroundings.

Relative Energies of NH_3 and/or NH_4^+ in the External and Internal Pore Sites. The 1.35 Å resolution structure (*17*) contains three partially resolved density peaks for nitrogen atoms in the Am2−Am4 internal pore positions of AmtB (Figure 4). In the following, we explore what species can enter the internal pore by computing free energies of the channel loading states potentially involved in the nitrogen transfer. The treatment here is limited to mutations of the occupancies at the external site, Am1, and the first pore position, Am2. The distance between the two sites is 9.7 Å. However, the transferred ammonia or ammonium probably travels an even greater distance since the (rotating) aromatic rings of Phe107 and Phe215 cross the straight linear path between the positions (Figure 4). The computed free energies are plotted in Figure 5 relative to state A, {H_2O/NH_3 NH_3 NH_3}, which is a useful reference for ammonium binding and a possible cyclic transport mechanism. State B, {H_2O/H_2O NH_3 NH_3}, where ammonia is replaced by a water molecule in pore site Am2, is higher in energy by 2.0 kcal/mol which demonstrates a significant affinity for ammonia at this site. States C and E, where ammonium ion binds to the Am1 position, are predicted to be more stable than state A by ∼6 kcal/mol. The relative free energies of hypothetical intermediate states D and F, resulting from the transfer of ammonium ion to Am2, hydration of Am1, and release of NH_3 to cytosol, are quite high, ∼22.0 kcal/mol (Figure 5). This also suggests that the apparent pK_a of NH_4^+ at the Am2 site decreases by ∼16 units compared to the normal pK_a of ammonium ion. The overall picture of nitrogen transfer becomes rather complex when translocation of water molecules together with NH_4^+ is additionally considered. As one can notice, states B−D involve translocation of a water molecule together with NH_4^+. Two lines of evidence could, in principle, support inclusion of water in the internal pore. First, the FEP/MD calculations show that state C, {NH_4^+/H_2O NH_3 NH_3}, with water at the Am2 site is 0.5 kcal/mol more stable than state E, {NH_4^+/NH_3 NH_3 NH_3}, with only ammonia species transported (Figure 5). Second, it is interesting to note that in the crystal structure the internal pore contains unoccupied empty space immediately near Phe215, which has a volume sufficient for inclusion of transient ammonia or a water molecule. A partial occupancy of this additional site was observed in a number of the MD trajectories. Interestingly, the results of the MM-PB calculations (*18*) using a continuum dielectric description with an ϵ_w of 80 for the channel pore predict that the NH_4^+ energy at the internal position near Phe215 is similar to the energy at the external binding site. In our calculations, the presence of a water molecule in the Am3 site does not provide any marked stabilization of the high-energy state D compared to state F. Furthermore, the X-ray structure and measurements of osmotic permeability show that water does not flow alone through the AmtB pore (*17*).

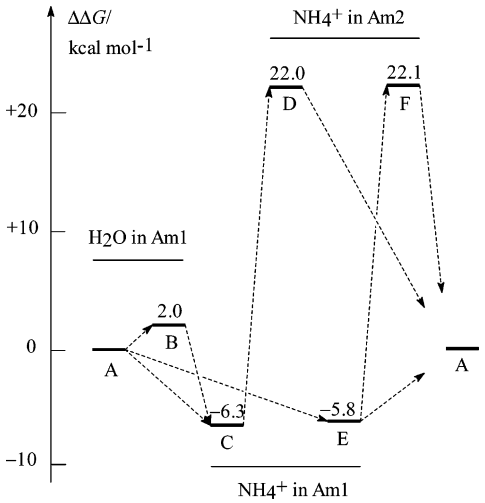

FIGURE 5: Relative free energies of the channel occupancy states: (A) {H_2O/NH_3 NH_3 NH_3}, (B) {H_2O/H_2O NH_3 NH_3}, (C) {NH_4^+/H_2O NH_3 NH_3}, (D) {H_2O/NH_4^+ H_2O NH_3}, (E) {NH_4^+/NH_3 NH_3 NH_3}, and (F) {H_2O/NH_4^+ NH_3 NH_3}. In braces are given the permeating species at experimental ammonia positions Am1−Am4, respectively, where the separation of the external Am1 site from the interior ones is indicated with a slash.

This study provides only a part of the whole picture of the permeation mechanism in AmtB, yet the described results indicate that the charged ammonia species are significantly destabilized (by more than 20 kcal/mol) in the channel interior compared with the neutral form (Figure 5). The

previous MM-PB calculations have similarly predicted lower energies for the internal neutral ammonia and a barrier of ~10 kcal/mol for ammonium ion permeation (*18*). Considering the computational results, one can argue that in the uptake of ammonium the transfers of NH_3 and H^+ follow different routes. This can remind one of the permeation mechanism in another family of membrane channels, aquaporins, which efficiently decouple neutral water and proton fluxes. If the transfer of ammonium ion through the AmtB internal pore were the case, the involved ammonia species or the H-bonded imidazoles of His168 and His318 would in principle form a proton wire for translocation of H^+. The conduction of proton along the hydrogen-bonded chains would necessarily require (*54*, *55*) reorientation of the ammonia molecules or the histidine side chains that are involved. Computer simulations of the corresponding energy barriers may be of interest for future studies. However, the computed free energies of the states with internal NH_4^+, like the molecular simulation results for H_2O and H_3O^+ in the aquaporin pore (*24*, *56*), predict that a high barrier for ammonium ion transfer in AmtB is a result of an essential loss of the charge self-energy.

CONCLUSIONS

In this work, we have used molecular dynamics and free energy perturbation methods to compute the free energies of substrate binding, permeation, and selectivity for the ammonium transporter from *E. coli*. The molecular simulation results predict an increase in the apparent pK_a for the bound external NH_4^+ by more than 4 units which clearly supports binding of ammonium ion and not neutral ammonia. The computed absolute binding free energy for the AmtB···NH_4^+ complex (at physiological pH) of −5.8 to −7.3 kcal/mol is in an excellent agreement with the experimental affinity for ammonium among the MEP/Amt channels (*4*, *10*, *17*). The calculations further show that AmtB is selective for NH_4^+ against monovalent metal cations by several kilocalories per mole. The bound NH_4^+ is stabilized at the binding site mainly by electrostatic interactions, in which case an important contribution is provided by the functionally important proximal Asp160. The interactions of ammonium ion with the cavity-lining aromatic rings of F107 and Trp148 are substantially less pronounced. The calculations predict stabilization of the anionic form of the buried Asp160 in the protein surrounding by several pK_a units. The simulated mutation of the highly conserved Asp160 to Asn leads to destabilization of NH_4^+ in the active site by ~10 kcal/mol and a consequent loss of binding. This result agrees with the experimental observations that mutations of Asp to a neutral Ala or Asn in position 160 remove the *E. coli* AmtB and Mep2 activities (*20*, *21*). The simulation results also predict a loss of binding for the external NH_4^+ when His100, His145, His156, and His350 at the periplasmic side of the channel are protonated. However, since the external histidines are not conserved among the proteins of the MEP/Amt/Rh family, the predicted pH dependence of the ammonium uptake may only be valid for the channel studied here.

The calculated free energies of the channel occupancy states, corresponding to transfer of external NH_3 and/or NH_4^+ to the first internal site, Am2, support an operation mechanism involving neutral ammonia. It is also interesting to note that the computed increment of the apparent pK_a for NH_4^+ changes from 4 to −16 pK_a units when moving from external binding site Am1 to Am2. This indicates that ammonium is deprotonated only after entering the constricted part of the channel pore. Such a conclusion apparently differs from the mechanism of NH_4^+ deprotonation at the external binding site described elsewhere (*17*). Further computational studies may elucidate the proton transfer mechanisms and plausible interference of the proton acceptor species in the nitrogen permeation pathways of AmtB.

REFERENCES

1. Marini, A. M., Vissers, S., Urrestarazu, A., and Andre, B. (1994) Cloning and expression of the MEP1 gene encoding an ammonium transporter in *Saccharomyces cerevisiae*, *EMBO J. 13*, 3456−3463.
2. Ninnemann, O., Jauniaux, J. C., and Frommer, W. B. (1994) Identification of a high-affinity NH_4^+ transporter from plants, *EMBO J. 13*, 3464−3471.
3. Marini, A. M., Urrestarazu, A., Beauwens, R., and Andre, B. (1997) The Rh (Rhesus) blood group polypeptides are related to NH_4^+ transporters, *Trends Biochem. Sci. 22*, 460−461.
4. von Wiren, N., Gazzarrini, S., Gojon, A., and Frommer, W. B. (2000) The molecular physiology of ammonium uptake and retrieval, *Curr. Opin. Plant Biol. 3*, 254−261.
5. Ludewig, U., von Wiren, N., Rentsch, D., and Frommer, W. B. (2001) Rhesus factors and ammonium: A function in efflux? *Genome Biol. 2*, 1010.1−1010.5.
6. Weiner, I. D. (2004) The Rh gene family and renal ammonium transport, *Curr. Opin. Nephrol. Hypertens. 13*, 533−540.
7. Conroy, M. J., Jamieson, S. J., Blakey, D., Kaufmann, T., Engel, A., Fotiadis, D., Merrick, M., and Bullough, P. A. (2004) Electron and atomic force microscopy of the trimeric ammonium transporter AmtB, *EMBO Rep. 5*, 1153−1158.
8. Thomas, G. H., Mullins, J. G. L., and Merrick, M. (2000) Membrane topology of the Mep/Amt family of ammonium transporters, *Mol. Microbiol. 37*, 331−344.
9. Siewe, R. M., Weil, B., Burkovski, A., Eikmanns, B. J., Eikmanns, M., and Krämer, R. (1996) Functional and genetic characterization of the (methyl)ammonium uptake carrier of *Corynebacterium glutamicum*, *J. Biol. Chem. 271*, 5398−5403.
10. Marini, A. M., Soussi-Boudekou, S., Vissers, S., and Andre, B. (1997) A family of ammonium transporters in *Saccharomyces cerevisiae*, *Mol. Cell. Biol. 17*, 4282−4293.
11. Meier-Wagner, J., Nolden, L., Jakoby, M., Siewe, R., Krämer, R., and Burkovski, A. (2001) Multiplicity of ammonium uptake systems in *Corynebacterium glutamicum*: Role of Amt and AmtB, *Microbiology 147*, 135−143.
12. Ludewig, U., von Wiren, N., and Frommer, W. B. (2002) Uniport of NH_4^+ by the root hair plasma membrane ammonium transporter LeAMT1;1, *J. Biol. Chem. 277*, 13548−13555.
13. Soupene, E., He, L., Yan, D., and Kustu, S. (1998) Ammonia acquisition in enteric bacteria: Physiological role of the ammonium/methylammonium transport B (AmtB) protein, *Proc. Natl. Acad. Sci. U.S.A. 95*, 7030−7034.
14. Soupene, E., Ramirez, R. M., and Kustu, S. (2001) Evidence that fungal MEP proteins mediate diffusion of the uncharged species NH_3 across the cytoplasmic membrane, *Mol. Cell. Biol. 21*, 5733−5741.
15. Soupene, E., Lee, H., and Kustu, S. (2002) Ammonium/methylammonium transport (Amt) proteins facilitate diffusion of NH_3 bidirectionally, *Proc. Natl. Acad. Sci. U.S.A. 99*, 3926−3931.
16. Winkler, F. K. (2006) Amt/MEP/Rh proteins conduct ammonia, *Pfluegers Arch. Eur. J. Physiol. 451*, 701−707.
17. Khademi, S., O'Connel, J., III, Remis, J., Robles-Colmenares, Y., Miercke, L. J. W., and Stroud, R. M. (2004) Mechanism of ammonia transport by Amt/MEP/Rh: Structure of AmtB at 1.35 Å, *Science 305*, 1587−1594.
18. Zheng, L., Kostrewa, D., Bernèche, S., Winkler, F. K., and Li, X. D. (2004) The mechanism of ammonia transport based on the crystal structure of AmtB of *Escherichia coli*, *Proc. Natl. Acad. Sci. U.S.A. 101*, 17090−17095.
19. Mayer, M., Schaaf, G., Mouro, I., Lopez, C., Colin, Y., Neumann, P., Cartron, J. P., and Ludewig, U. (2006) Different transport mechanisms in plant and human AMT/Rh-type ammonium transporters, *J. Gen. Physiol. 127*, 133−144.

20. Javelle, A., Severi, E., Thornton, J., and Merrick, M. (2004) Ammonium sensing in *Escherichia coli*, *J. Biol. Chem. 279*, 8530−8538.
21. Marini, A. M., Boeckstaens, M., Benjelloun, F., Chérif-Zahar, B., and Andre, B. (2006) Structural involvement in substrate recognition of an essential aspartate residue conserved in Mep/Amt and Rh-type ammonium transporters, *Curr. Genet. 49*, 364−374.
22. Åqvist, J., and Luzhkov, V. (2000) Ion permeation mechanisms of the potassium channel, *Nature 404*, 881−884.
23. Luzhkov, V. B., and Åqvist, J. (2001) K^+/Na^+ selectivity of the KcsA potassium channel from microscopic free energy perturbation calculations, *Biochim. Biophys. Acta 1548*, 194−202.
24. Kato, M., Pislyakov, A. V., and Warshel, A. (2006) The barrier for proton transport in aquaporins as a challenge for electrostatic models: The role of protein relaxation in mutational calculations, *Proteins*, *64*, 829−844.
25. Liu, Y., and Hu, X. (2006) Molecular determinants for binding of ammonium ion in the ammonia transporter AmtB: A quantum mechanical study, *J. Phys. Chem. A 110*, 1375−1381.
26. Marelius, J., Kolmodin, K., Feierberg, I., and Åqvist, J. (1999) Q: A molecular dynamics program for free energy calculations and empirical valence bond simulations in biomolecular systems, *J. Mol. Graphics Modell. 16*, 213−225.
27. Kaminski, G. A., Friesner, R. A., Tirado-Rives, J., and Jorgensen, W. L. (2001) Evaluation and reparametrization of the OPLS-AA force field for proteins via comparison with accurate quantum chemical calculations on peptides, *J. Phys. Chem. B 105*, 6474−6487.
28. Martinez, J. M., and Martinez, L. (2003) Packing optimization for automated generation of complex system's initial configurations, *J. Comput. Chem. 24*, 819−825.
29. Lee, F. S., and Warshel, A. (1992) A local reaction field method for fast evaluation of long-range electrostatic interactions in molecular simulations, *J. Chem. Phys. 97*, 3100−3107.
30. Åqvist, J., Wennerström, P., Nervall, M., Bjelic, S., and Bransdal, B. O. (2004) Molecular dynamics simulations of water and biomolecules with a Monte Carlo constant pressure algorithm, *Chem. Phys. Lett. 384*, 288−294.
31. King, G., and Warshel, A. (1989) A surface constrained all-atom solvent model for effective simulations of polar solutions, *J. Chem. Phys. 91*, 3647−3661.
32. van Gunsteren, W. F., and Berendsen, H. J. C. (1990) Computer simulation of molecular dynamics: Methodology, applications, and perspectives in chemistry, *Angew. Chem., Int. Ed. 29*, 992−1023.
33. Kollman, P. (1993) Free energy calculations: Applications to chemical and biochemical phenomena, *Chem. Rev. 93*, 2395−2417.
34. Brandsdal, B. O., Österberg, F., Almlöf, M., Feiegberg, I., Luzhkov, V. B., and Åqvist, J. (2003) Free energy calculations and ligand binding, *Adv. Protein Chem. 66*, 123−158.
35. Bernèche, S., and Roux, B. (2001) Energetics of ion conduction through the K^+ channel, *Nature 414*, 73−77.
36. Luzhkov, V. B., and Åqvist, J. (2005) Ions and blockers in potassium channels: Insights from free energy simulations, *Biochim. Biophys. Acta 1747*, 109−120.
37. Zacharias, M., Straatsma, T. P., and McCammon, J. A. (1994) Separation-shifted scaling, a new scaling method for Lennard-Jones interactions in thermodynamic integration, *J. Chem. Phys. 100*, 9025−9031.
38. Lee, F. S., Chu, Z. T., and Warshel, A. (1992) Calculations of antibody−antigen interactions: Microscopic and semi-microscopic evaluation of the free energies of binding of phosphorylcholine analogs to McPC603, *Protein Eng. 5*, 215−228.
39. Åqvist, J., Medina, C., and Samuelsson, J. E. (1994) A new method for predicting binding affinity in computer-aided drug design, *Protein Eng. 7*, 385−391.
40. Jorgensen, W. L., and Gao, J. (1986) Monte Carlo simulations of the hydration of ammonium and carboxylate ions, *J. Phys. Chem. 90*, 2174−2182.
41. Rizzo, R. C., and Jorgensen, W. L. (1999) OPLS all-atom model for amines: Resolution of the amine hydration problem, *J. Am. Chem. Soc. 121*, 4827−4836.
42. Oostenbrink, C., Juchli, D., and van Gunsteren, W. F. (2005) Amine hydration: A united-atom force-field solution, *ChemPhysChem 6*, 1800−1804.
43. Luzhkov, V. B., Österberg, F., Acharaya, P., Chattopadhyaya, J., and Åqvist, J. (2002) Computational and NMR study of quaternary ammonium ion conformations in solution, *Phys. Chem. Chem. Phys. 4*, 4640−4647.
44. Ben-Naim, A., and Marcus, Y. (1984) Solvation thermodynamics of nonionic solutes, *J. Chem. Phys. 81*, 2016−2027.
45. Rosseinsky, D. R. (1965) Electrode potentials and hydration energies, theories and correlations, *Chem. Rev. 65*, 467−490.
46. Klots, C. E. (1981) Solubility of protons in water, *J. Phys. Chem. 85*, 3585−3588.
47. Åqvist, J. (1990) Ion−water interaction potentials derived from free energy perturbation simulations, *J. Phys. Chem. 94*, 8021−8024.
48. Luzhkov, V. B., and Åqvist, J. (2000) A computational study of ion binding and protonation states in the KcsA potassium channels, *Biochim. Biophys. Acta 1481*, 360−370.
49. Bernèche, S., and Roux, B. (2002) The ionization state and the conformation of Glu-71 in the KcsA K^+ channel, *Biophys. J. 82*, 772−780.
50. Warshel, A. (1981) Calculations of enzymatic reactions: Calculations of pK_a, proton-transfer reactions, and general acid catalysis reactions in enzymes, *Biochemistry 20*, 3167−3177.
51. Åqvist, J., and Warshel, A. (1989) Energetics of ion permeation through membrane channels. Solvation of Na^+ by gramicidin A, *Biophys. J. 56*, 171−182.
52. Marcus, Y. (1988) Ionic radii in aqueous solutions, *Chem. Rev. 88*, 1475−1498.
53. Johnson, D. A. (2000) Thermochemical aspects of the rotational dynamics of the ammonium ion in an environment of water molecules, *ChemPhysChem 2*, 2903−2906.
54. Nagle, J. F., and Morowitz, H. J. (1978) Molecular mechanisms for proton transport in membranes, *Proc. Natl. Acad. Sci. U.S.A. 75*, 298−302.
55. Nagle, J. F., and Mille, M. (1978) Molecular models of proton pumps, *J. Chem. Phys. 74*, 1367−1372.
56. Burykin, A., and Warshel, A. (2003) What really prevents proton transport through aquaporin? Charge self-energy versus proton wire proposal, *Biophys. J. 85*, 3696−3706.

BI0610799